Solid State Communications 151 (2011) 1100–1104

Contents lists available at ScienceDirect

Solid State Communications

journal homepage: www.elsevier.com/locate/ssc

Electronic properties of grains and grain boundaries in graphene grown by chemical vapor deposition

Luis A. Jauregui [a,b], Helin Cao [a,c], Wei Wu [d,e], Qingkai Yu [d,e,f], Yong P. Chen [c,a,b,*]

[a] Birck Nanotechnology Center, Purdue University, West Lafayette, IN 47907, USA
[b] School of Electrical and Computer Engineering, Purdue University, West Lafayette, IN 47907, USA
[c] Department of Physics, Purdue University, West Lafayette, IN 47907, USA
[d] Center for Advanced Materials, University of Houston, Houston, TX 77204, USA
[e] Department of Electrical and Computer Engineering, University of Houston, Houston, TX 77204, USA
[f] Ingram School of Engineering and Materials Science, Engineering and Commercialization Program, Texas State University, San Marcos, TX 78666, USA

ARTICLE INFO

Article history:
Accepted 15 May 2011
by V. Fal'ko
Available online 25 May 2011

Keywords:
A. Graphene
B. Chemical vapor deposition
C. Grain boundary
D. Electronic transport

ABSTRACT

We synthesize hexagonal shaped single-crystal graphene, with edges parallel to the zig-zag orientations, by ambient pressure CVD on polycrystalline Cu foils. We measure the electronic properties of such grains as well as of individual graphene grain boundaries, formed when two grains merged during the growth. The grain boundaries are visualized using Raman mapping of the *D* band intensity, and we show that individual boundaries between coalesced grains impede electrical transport in graphene and induce prominent weak localization, indicative of intervalley scattering in graphene.

1. Introduction

Since its discovery, graphene has attracted a lot of attention in many fields. Graphene's potential applications have motivated the development of large-scale synthesis of graphene grown by several methods, including graphitization of SiC surfaces [1,2] and chemical vapor deposition (CVD) on transition metals such as Ni [3–5] and Cu [6]. In particular, it has been shown that large and predominantly monolayer graphene of excellent quality can be synthesized by CVD on polycrystalline Cu foils [6–8]. This relatively simple and low-cost method has been used to produce graphene that can reach impressive sizes [7] and can be easily transferred to other substrates [7,9]. So far, all of the large-scale synthetic graphene films produced are polycrystalline [10–14], consisting of many single-crystalline grains separated by grain boundaries formed when grains coalesced. The grain boundaries (which, by definition, are defective) degrade the electrical [12,14–16] properties of the resulting films. In order for graphene to realize its promise in "carbon-based" electronics, progresses have been made to synthesize either large-scale, high-quality single-crystalline graphene films [17], or to achieve better control over the nucleation of individual graphene grains and to avoid the grain boundaries in fabricated graphene devices [16].

Recently, we have studied the growth of hexagonal shaped graphene grains by ambient pressure CVD. We have shown by transmission electron microscopy and scanning tunneling microscopy studies that the edges of graphene grains are preferably oriented along the zig-zag direction. Additionally, we studied grains and grain boundaries by Raman and electrical measurements [16]. Here we present further results from electrical transport measurements of graphene grains and grain boundaries, primarily how individual grain boundaries impede electronic transport and scatter charge carriers.

2. Experimental details

The graphene studied in this work is synthesized on polycrystalline Cu foils by ambient pressure CVD. First, a Cu foil (25-μm-thick, 99.8%, Alfa Aesar) is loaded into a CVD furnace and heated up to 1050 °C under 300 sccm Ar and 10 sccm H_2. After reaching 1050 °C, the sample is annealed for 30 min or longer without changing the gas flow rates. The growth is then carried out at 1050 °C for ∼10 min under a gas mixture of 300 sccm diluted (in Ar) CH_4 (concentration 8 ppm) and 10 sccm of H_2. We halt growth before the graphene grains merge with each other to form a globally continuous (but polycrystalline) graphene film [8,18]. Finally,

* Corresponding author at: Department of Physics, Purdue University, West Lafayette, IN 47907, USA. Tel.: +1 765 494 0947; fax: +1 765 494 0706.
E-mail address: yongchen@purdue.edu (Y.P. Chen).

0038-1098/$ – see front matter © 2011 Elsevier Ltd. All rights reserved.
doi:10.1016/j.ssc.2011.05.023

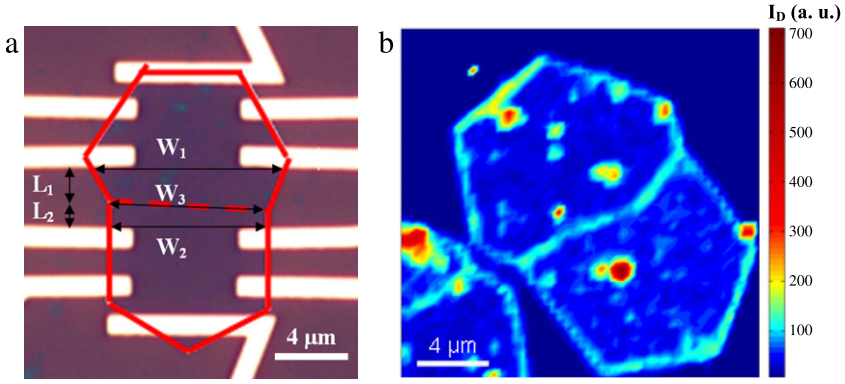

Fig. 1. (a) Optical image of multi-terminal device on two merged graphene grains. (b) Raman mapping of the *D* band intensity (I_D) for the sample depicted in (a) prior to the device fabrication.

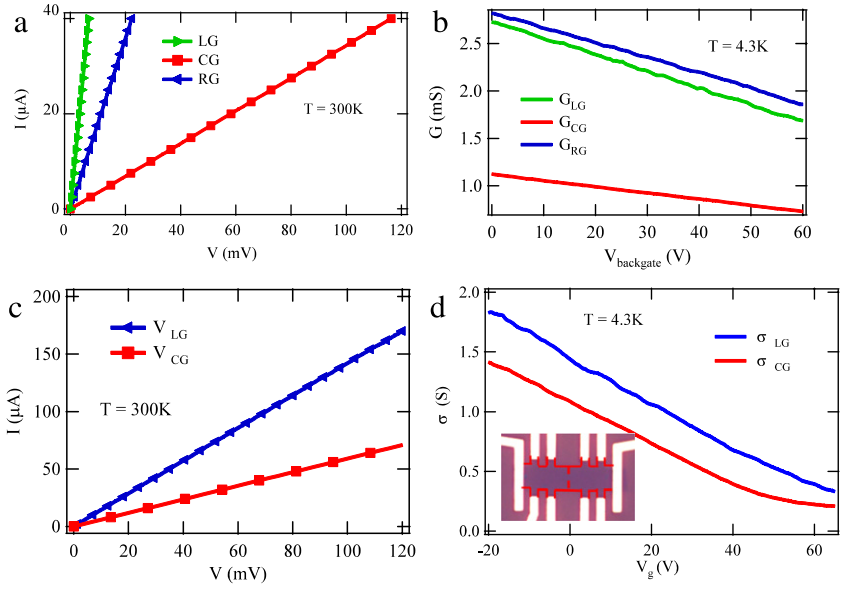

Fig. 2. (a, b) *I*–*V* and field effect in conductance curves measured within each graphene grain (left and right grains) and across the grain boundary for a device similar to the one shown in Fig. 1(a). (c, d) *I*–*V* and field effect in conductivity ($\sigma = G(L/W)$) curves measured within a graphene grain (left grain) and across the grain boundary for a Hall bar (width = 2.5 μm) patterned device depicted in the inset of Fig. 2(d). All the measurements are performed at zero magnetic field using 4-probe configurations. The sub-indexes LG, RG, and CG refer to left, right, and cross grain respectively. The field effect curves are measured at low temperature to suppress gate leakage.

the sample is rapidly cooled to room temperature under the protection of Ar and H_2, and then taken out of the furnace. Graphene samples are transferred by a PMMA (polymethyl methacrylate) assisted process in a Cu etchant (iron nitrate) onto SiO_2/Si wafers (doped Si covered by 300 nm SiO_2) for Raman and electrical transport studies. The graphene grains are typically hexagonally shaped, with ∼120° corners, and their edges are shown to be parallel to the zig-zag directions [16]. The hexagonal shape is notably different from the flower-like shape of previously reported graphene grains grown by low pressure CVD [6,12,19].

After transferring graphene grains from the Cu foil to SiO_2 by the PMMA method, we protect the chosen grains or pair of merged grains by negative e-beam resist (MA-N 2403). Then, we etch everywhere else by O_2 plasma etching, to avoid shortening of the electrical contacts by other graphene grains. The electrical contacts (Cr/Au, 5 nm/35 nm, e-beam evaporated) to graphene grains are patterned by *e*-beam lithography. The resistances are measured using low frequency lock-in detection (Stanford Research 830) with a driving current of 1 μA. DC *I*–*V* curves are measured with a DC source meter (Keithley 2400). The highly doped silicon substrate is used as a backgate. All the electrical transport data in the main text are taken in vacuum (∼10^{-5} Torr) in a variable temperature probe station (Lakeshore CPX-VF). The low temperature high field magnetotransport data in Fig. 6(a) and (b) are measured in a He-3 superconducting magnet system at the National High Magnetic Field Laboratory (NHMFL).

3. Results and discussion

Fig. 1(a) shows a typical device with multi-terminal electrodes on merged graphene grains that allow us to measure intra-grain (within grain) and inter-grain (across graphene grain boundary) electrical properties. Fig. 1(b) shows the Raman mapping of the *D* band intensity of the sample represented in Fig. 1(a) before device fabrication. An intense Raman *D*-peak can be detected between graphene grains corresponding to the graphene grain boundary [16].

Fig. 2(a) shows the *I*–*V* curves measured at room temperature for a device similar to the one shown in Fig. 1(a). From the *I*–*V* curves, the conductance across the grain boundary is found to be less than the conductance of each individual grain (left or right). Conductance across the grain boundary is lower than the conductance of each grain at different carrier densities (n_0) tuned by the backgate voltage (V_g), as shown in Fig. 2(b). Even

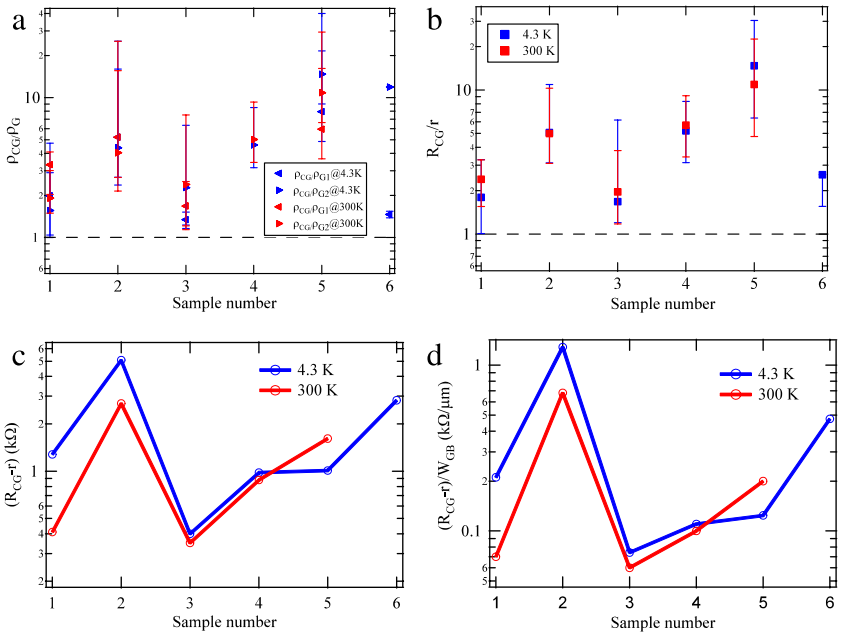

Fig. 3. (a) ρ_{CG}/ρ_G ratio between inter-grain resistivity (ρ_{CG}) and intra-grain resistivity (ρ_G) for various samples. (b) Ratio (R_{CG}/r) between measured inter-grain resistance (R_{CG}) and calculated (neglecting the grain boundary) inter-grain series resistance (r). (c) Effective grain boundary resistance ($R_{CG}-r$). (d) Effective grain boundary resistance per unit length of grain boundary (W_{GB}). W_{GB} is the length of the grain boundary (e.g. W_3 in Fig. 1(a)).

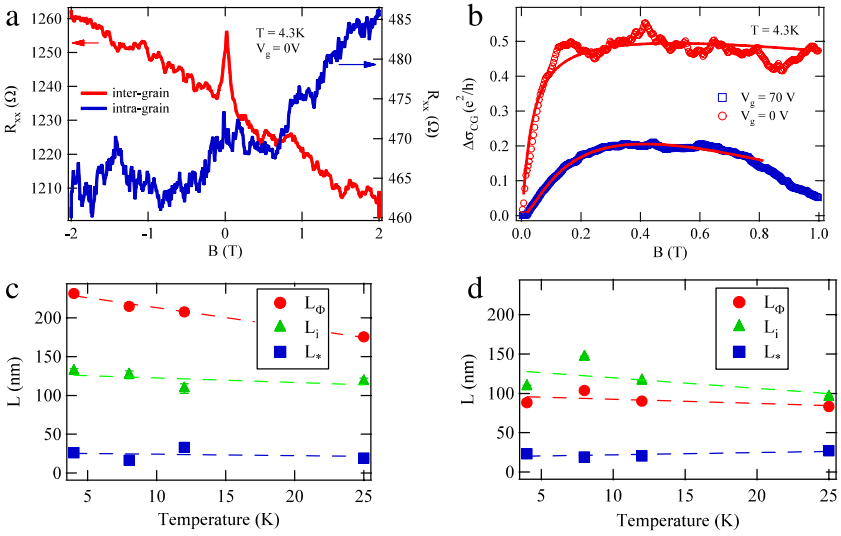

Fig. 4. (a) Low field magnetoresistances measured at 4.3 K and backgate voltage $V_g = 0$ V. (b) Magnetoconductivity and its respective weak localization fittings (solid lines) for $T = 4.3$ K and at $V_g = 0$ V and $V_g = 70$ V. (c, d) Characteristic lengths extracted from such fittings for data measured at various temperatures and two different carrier densities $\sim 5.0 \times 10^{12}$ cm^{-2} ($V_g = 0$ V) and near the Dirac point ($V_g \sim 70$ V) respectively. All measurements where performed on the device depicted in the inset of Fig. 2(d).

after considering the device geometry, the effective cross-grain conductivity is still lower than within the grain. Similar results are also found on one pair of merged graphene grains patterned into a Hall bar structure with uniform width, and an optical image of the device is shown in the inset of Fig. 2(d). So far, all the devices we have measured are p-type doped (likely due to adsorbates from the environment and residues from the transfer and device fabrication processes), and the Dirac point is not reached within the range of backgate voltage (up to 60 V) used.

We have measured the intra-grain (R_G) and inter-grain (R_{CG}) resistances for several different devices. Taking into account the device geometry, we can extract an effective resistivity, $\rho_{CG} = R_{CG}/(L/W_a)$, where W_a and L are defined as $\frac{1}{W_a} = \frac{1}{L}\int_0^L \frac{dx}{W(x)}$ and $L = L_1 + L_2$ (Fig. 1(a)), respectively [16]. The inter-grain resistivity is higher than both of the intra-grain resistivities (ρ_L for the left grain and ρ_R for the right grain) for all the devices, as depicted in Fig. 3(a), indicating that the grain boundary impedes the electric transport. We can also calculate an inter-grain series resistance $\left(r = \rho_L \int_0^{L_1} \frac{dx}{W(x)} + \rho_R \int_{L_1}^{L} \frac{dx}{W(x)}\right)$ that neglects the grain boundary, by simply integrating the intra-grain resistivities [16]. This gives an r significantly smaller than the measured R_{CG}, indicating that the grain boundary provides an "extra" resistance (Fig. 3(b)). We have found qualitatively similar results in all of the coalesced grain devices we have measured (Fig. 3(a) and (b)): inter-grain resistivities (ρ_{CG}) are always higher than corresponding intra-grain resistivities (ρ_G, on each side of the grain boundary), and R_{CG} is always higher than the calculated r. Additionally, we have extracted the effective grain boundary resistance ($R_{CG} - r$) and its value per unit length of grain boundary as depicted in Fig. 3(c) and (d) respectively.

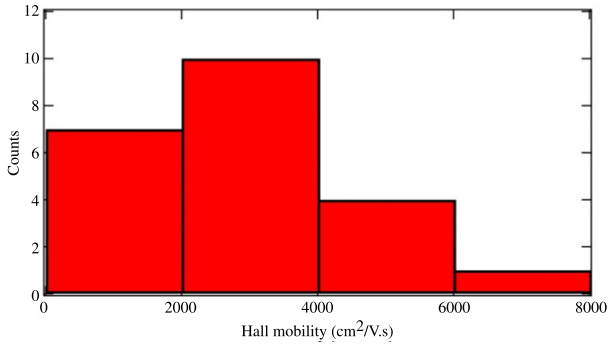

Fig. 5. Hall mobility histogram for a series of graphene grain devices, the measurement is performed at 4.3 K and $V_g = 0$ V. Some of the grains are grown by a seeded process [16].

Magnetotransport measurements are performed under a perpendicular magnetic field (B). Fig. 4(a) presents low temperature (4.3 K) magnetoresistance ($R_{xx}(B)$) measured across the grain boundary compared to $R_{xx}(B)$ measured within one of the graphene grains. The inter-grain $R_{xx}(B)$ displays a prominent peak at $B = 0$ T, associated with weak localization (WL). Such a WL peak is much weaker or even unobservable for intra-grain $R_{xx}(B)$. WL results from an interplay between impurity scattering and quantum coherent transport of carriers (such interplay also leads to reproducible "universal conductance fluctuations" (UCF) in the resistance, which are also observable in our devices). Raising the temperature (T) destroys the phase coherence, and therefore diminish the WL feature, as was indeed observed in our samples [16]. In graphene, due to the chiral nature of carriers, WL requires the presence of sharp defects that cause intervalley scattering with large momentum (q) transfer. Our observation of prominent inter-grain WL but much weaker or negligible intra-grain WL indicates that grain boundaries are major sources of intervalley scattering in our graphene devices (where inter-grain current has to cross the grain boundary), while such scattering is less significant within the single-crystal graphene grains.

The inter-grain WL feature we observe at low temperature can be well fitted to the WL theory developed for graphene [20]. Fig. 4(b), shows the cross-grain boundary (CG) magnetoconductivity ($\Delta\sigma_{CG}(B) = \sigma_{CG}(B) - \sigma_{CG}(B = 0)$), normalized by e^2/h and antisymmetrized to eliminate the small Hall component. We present corresponding weak localization fittings for two different carrier densities. From the fitting at different temperatures, we extract various inelastic (L_φ, phase-breaking) and elastic (L_i, intervalley; and L_*, intravalley) scattering lengths for carrier densities of $\sim 5.0 \times 10^{12}$ cm^{-2} ($V_g = 0$ V) and near the Dirac point ($V_g \sim 70$ V), as shown in Fig. 4(c) and (d) respectively. There is no significant variation of elastic scattering lengths (L_i and L_*) for different carrier densities, however the L_φ measured at 4.3 K decreases from $\sim$250 nm for $V_g = 0$ V to $\sim$100 nm for $V_g = 70$ V. A similar variation was reported in Ref. [21]. Electron–hole puddles, formed near Dirac point, can be one cause of this reduction, as suggested in an earlier study in Ref. [22]. It has been suggested that puddles can produce fluctuating electromagnetic fields, that enhances the inelastic scattering [21]. Furthermore, we extract the phase-breaking rate (τ_ϕ) by $\tau_\phi^{-1} = D/L_\phi^2$, where D is the diffusion coefficient ($D = v_F l/2$, here v_F is the Fermi velocity, $l = h/(2\rho_{CG}e^2\sqrt{\pi n_0})$ is the mean free path, e is the elementary electric charge, and h is the Plank's constant). We obtain for $V_g = 70$ V (near Dirac point) and $V_g = 0$ V phase-breaking rates of 3.91 ps^{-1} and 0.36 ps^{-1} respectively at 4.3 K.

The intra-grain mobility (μ_G) extracted from low temperature Hall measurements in all of the devices we studied (fabricated on isolated as well as coalesced grains) ranged from $<10^3$ cm^2/V s to $\sim 10^4$ cm^2/V s as shown in Fig. 5. Inter-grain mobility is not extracted as the two coalescing grains often had different carrier densities (in the cases where their densities are comparable, the inter-grain mobility is lower than μ_G by similar factors as the resistivity ratios shown in Fig. 3(a)). Our work has clearly indicated the detrimental effect of grain boundaries on electronic transport, and that avoiding grain boundaries is beneficial for improving the mobility. However, the wide variation of μ_G in different samples (sometimes even between neighboring grains) and the occasional low μ_G observed suggest that other sources of disorder could also strongly affect the mobilities. Such "extra" disorder may also be partially responsible for the small intravalley scattering length ($L_* < 30$ nm, Fig. 4(c) and (d)) observed (indicating a significant amount of small-q scattering defects such as charged impurities, line defects and ripples etc. that may arise from, e.g. graphene transfer or device fabrication processes). Improving related fabrication processes to reduce such defects will be required to achieve consistent high mobilities in graphene-based devices.

We have studied the quantum Hall effect (QHE) in the intra-grain and inter-grain Hall resistances, measured under high magnetic fields and low temperatures (450 mK), as shown in Fig. 6(a) and (b) respectively. For the intra-grain Hall resistance (Fig. 6(a)), we observe quantized or developing R_{xy} plateaus at $e^2/10h$, $e^2/14h$, $e^2/18h$, $e^2/22h$, corresponding to the Landau level (LL) filling factors $\nu = 10, 14, 18, 22$ respectively. For the inter-grain Hall resistance (Fig. 6(b)) we observe a quantized R_{xy} plateau at $e^2/6h$, corresponding to $\nu = 6$. Such half integer quantum Hall effect, where $\nu = 4(n + 1/2)$ (n is a non-negative integer), first observed in exfoliated graphene [23,24] and also later in CVD graphene [3,7,8], reflects the electronic properties of chiral massless Dirac fermions in graphene. The intra-grain and average inter-grain carrier densities for the samples measured in Fig. 6(a) and (b) are $\sim 4.4 \times 10^{12}$ cm^{-2} and $\sim 1.9 \times 10^{12}$ cm^{-2} respectively.

4. Conclusions

Grain boundaries can reduce the electrical conductivity of polycrystalline graphene. The presence of a graphene grain boundary can be visualized by the mapping the intensity of the

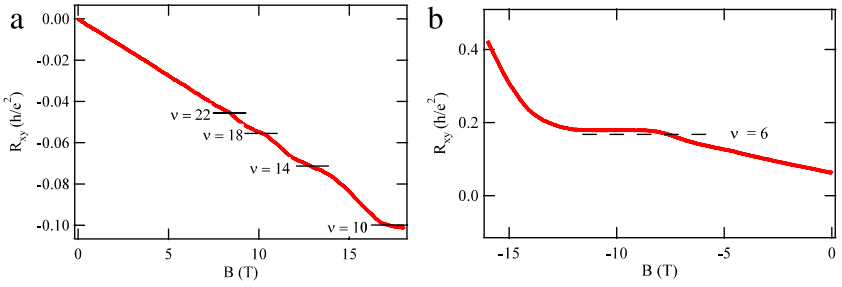

Fig. 6. Intra-grain (a) and inter-grain (b) Hall resistance (R_{xy}) for 2 different devices shows Quantum Hall effect of monolayer graphene. Temperature in both cases is 450 mK.

Raman *D*-band. This *D*-band comes from an intervalley scattering process, which involves the presence of sharp defects, such as grain boundaries. Weak localization is found in the measurement of the inter-grain magnetoresistance, suggesting that grain boundaries causes intervalley scattering. For our sample, carrier mobility of the grains shows a wide variation, maybe due to the uncontrollable amount of disorder introduced during the transferring and device fabrication process. Electrical measurements under high magnetic fields show the characteristic quantum Hall effect of single layer graphene, within graphene grains and across the grain boundary.

Acknowledgments

QY acknowledges support from NSF and CAM Special Funding. YPC acknowledges support from NSF, DTRA, DHS, IBM, Miller Family Endowment, Midwest Institute for Nanoelectronics Discovery (MIND). Parts of the measurements were performed at the National High Magnetic Field Laboratory (supported by NSF, DOE and the State of Florida) and the authors thank E. Palm and G. Jones for experimental assistance.

References

[1] W.A. de Heer, C. Berger, X.S. Wu, P.N. First, E.H. Conrad, X.B. Li, T.B. Li, M. Sprinkle, J. Hass, M.L. Sadowski, M. Potemski, G. Martinez, Solid State Commun. 143 (2007) 92.
[2] K.V. Emtsev, A. Bostwick, K. Horn, J. Jobst, G.L. Kellogg, L. Ley, J.L. McChesney, T. Ohta, S.A. Reshanov, J. Rohrl, E. Rotenberg, A.K. Schmid, D. Waldmann, H.B. Weber, T. Seyller, Nat. Mater. 8 (2009) 203.
[3] K.S. Kim, Y. Zhao, H. Jang, S.Y. Lee, J.M. Kim, J.H. Ahn, P. Kim, J.Y. Choi, B.H. Hong, Nature 457 (2009) 706.
[4] A. Reina, X.T. Jia, J. Ho, D. Nezich, H.B. Son, V. Bulovic, M.S. Dresselhaus, J. Kong, Nano Lett. 9 (2009) 30.
[5] Q.K. Yu, J. Lian, S. Siriponglert, H. Li, Y.P. Chen, S.S. Pei, Appl. Phys. Lett. 93 (2008) 113103.
[6] X.S. Li, W.W. Cai, J.H. An, S. Kim, J. Nah, D.X. Yang, R. Piner, A. Velamakanni, I. Jung, E. Tutuc, S.K. Banerjee, L. Colombo, R.S. Ruoff, Science 324 (2009) 1312.
[7] S. Bae, H. Kim, Y. Lee, X.F. Xu, J.S. Park, Y. Zheng, J. Balakrishnan, T. Lei, H.R. Kim, Y.I. Song, Y.J. Kim, K.S. Kim, B. Ozyilmaz, J.H. Ahn, B.H. Hong, S. Iijima, Nat. Nanotechnol. 5 (2010) 574.
[8] H.L. Cao, Q.K. Yu, L.A. Jauregui, J. Tian, W. Wu, Z. Liu, R. Jalilian, D.K. Benjamin, Z. Jiang, J. Bao, S.S. Pei, Y.P. Chen, Appl. Phys. Lett. 96 (2010) 122106.
[9] Y.P. Chen, Q.K. Yu, Nat. Nanotechnol. 5 (2010) 559.
[10] P.Y. Huang, C.S. Ruiz-Vargas, A.M.v.d. Zande, W.S. Whitney, S. Garg, J.S. Alden, C.J. Hustedt, Y. Zhu, J. Park, P.L. McEuen, D.A. Muller, Nature 469 (2011) 389.
[11] K. Kim, Z. Lee, W. Regan, C. Kisielowski, M.F. Crommie, A. Zettl, ACS Nano. 5 (2011) 2142.
[12] X.S. Li, C.W. Magnuson, A. Venugopal, J. An, J.W. Suk, B. Han, M. Borysiak, W. Cai, A. Velamakanni, Y. Zhu, L. Fu, E.M. Vogel, E. Voelkl, L. Colombo, R.S. Ruoff, Nano Lett. 10 (2010) 4328.
[13] Y.Y. Liu, B.I. Yakobson, Nano Lett. 10 (2010) 2178.
[14] O.V. Yazyev, S.G. Louie, Nat. Mater. 9 (2010) 806.
[15] O.V. Yazyev, S.G. Louie, Phys. Rev. B 81 (2010) 195420.
[16] Q. Yu, L.A. Jauregui, W. Wu, R. Colby, J. Tian, Z. Su, H. Cao, Z. Liu, D. Pandey, D. Wei, T.F. Chung, P. Peng, N. Guisinger, E.A. Stach, J. Bao, S.-s. Pei, Y.P. Chen, Nat. Mater. 10 (2011) 443.
[17] X.S. Li, C.W. Magnuson, A. Venugopal, R.M. Tromp, J.B. Hannon, E.M. Vogel, L. Colombo, R.S. Ruoff, J. Am. Chem. Soc. 133 (2011) 2816.
[18] W. Wu, Z.H. Liu, L.A. Jauregui, Q.K. Yu, R. Pillai, H.L. Cao, J.M. Bao, Y.P. Chen, S.S. Pei, Sensors Actuators B: Chem. 150 (2010) 296.
[19] X.S. Li, W.W. Cai, L. Colombo, R.S. Ruoff, Nano Lett. 9 (2009) 4268.
[20] E. McCann, K. Kechedzhi, V.I. Fal'ko, H. Suzuura, T. Ando, B.L. Altshuler, Phys. Rev. Lett. 97 (2006) 146805.
[21] D.-K. Ki, D. Jeong, J.-H. Choi, H.-J. Lee, Phys. Rev. B 78 (2008) 125409.
[22] F.V. Tikhonenko, D.W. Horsell, R.V. Gorbachev, A.K. Savchenko, Phys. Rev. Lett. 100 (2008) 056802.
[23] K.S. Novoselov, A.K. Geim, S.V. Morozov, D. Jiang, M.I. Katsnelson, I.V. Grigorieva, S.V. Dubonos, A.A. Firsov, Nature 438 (2005) 197.
[24] Y. Zhang, Y.W. Tan, H.L. Stormer, P. Kim, Nature 438 (2005) 201.